Applied Surface Science Advances 13 (2023) 100352

Contents lists available at ScienceDirect

Applied Surface Science Advances

journal homepage: www.sciencedirect.com/journal/applied-surface-science-advances

Characterizations of extrinsically doped CZTS thin films for solar cell absorbers fabricated by sol-gel spin coating method

Ashoke Kumar Sen Gupta[a,*], Syed Farid Uddin Farhad[b,c], Md. Shehan Habib[b,c], Mohammad Robiul Hossan[d], Khalid Hossain[e], Nipu Kumar Das[a], Muhammad Quamruzzaman[a], M.A. Matin[a], N. Amin[f,g]

[a] *Department of Electrical and Electronic Engineering, Renewable Energy Laboratory, Chittagong University of Engineering and Technology (CUET), Chattogram 4349, Bangladesh*
[b] *Energy Conversion and Storage Research Section, Industrial Physics Division, BCSIR Labs, Bangladesh Council of Scientific and Industrial Research (BCSIR), Dhaka 1205, Bangladesh*
[c] *Central Analytical and Research Facilities (CARF), Bangladesh Council of Scientific and Industrial Research (BCSIR), Dhaka 1205, Bangladesh*
[d] *Department of Engineering and Physics, University of Central Oklahoma, Edmond, OK 73034, USA*
[e] *JP Analytical LLC, 459 Case Circle, Ardmore, OK 73401, USA*
[f] *Faculty of Engineering and Built Environment, Universiti Kebangsaan Malaysia (The National University of Malaysia) Bangi, Selangor 43600, Malaysia*
[g] *Institute of Sustainable Energy, Universiti Tenaga Nasional (The National Energy University), Jalan IKRAM-UNITEN, Kajang, Selangor 43000, Malaysia*

ARTICLE INFO

Keywords:
Characterizations
CZTS
Thin film
Extrinsically doped
Spin coating

ABSTRACT

In copper zinc tin sulfide (CZTS) based thin films, copper zinc antisite (Cu_{Zn}) represents the major p-type acceptor defect with low formation energy. This antisite can create defect-dominated carrier recombination hotspots, which reduces power conversion efficiency. Extrinsic doping in cationic sites of the CZTS thin film during synthesis is an effective way to passivate this defect. It has previously been reported that employing Cd as a dopant can passivate this defect and improve film quality. Injecting toxic Cd into non-toxic CZTS may create more problems than it solves. Simultaneous doping of Cd and other atoms like Mg is hypothesized to accomplish this goal of lowering Cd concentration. For this, it is important to know the effect of doping Cd and Mg separately under analogous experimental conditions. The structural, morphological, and optical properties, as well as the chemical bonding states, of sol-gel spin-coated CZTS thin films were investigated in this study using independent and controlled Cd and Mg doping. The fabrication procedure consisted of two steps: sol-gel spin coating followed by sulfurization. As a solvent for precursors in creating sols for spin coating processes, dimethyl sulfoxide (DMSO) was employed. Each dopant's precursor concentration was chosen to ensure an identical mole percentage of zinc precursor in the solution. The fabricated films were characterized undoped and doped forms using X-ray diffractometry (XRD) with Rietveld refinements, Raman spectroscopy, Field emission scanning electron microscopy (FESEM), 3D profilometry, and Ultraviolet-visible near-infrared (UV-Vis NIR) spectroscopy. The elemental composition ratio and chemical bonding states of the fabricated films were probed by Energy dispersive X-ray spectroscopy (EDS) and X-ray photoelectron spectroscopy (XPS), respectively. Fabricated thin films exhibit distinct synergistic features depending on the dopant types used in the fabrication process. The crystal structure of the doped absorber and the chemical valence states of the other elements (Cu, Zn, Sn, and S) were not changed as shown by XRD, Raman, and XPS analyses. The main diffraction peak at the (112) plane is found at Bragg's diffraction angle of 28.6° for an undoped sample. This peak shifts left upon Cd and Mg doping to 28.2° and 28.4° owing to different ionic radii of dopants relative to Zn ions, which indicates the presence of dopants in the fabricated films. Raman spectroscopy probes the Cu-Sn-S secondary phases: cubic Cu_2SnS_3 at 305 cm^{-1} in the undoped sample, tetragonal Cu_2SnS_3 at 296 cm^{-1} in the Cd-doped sample, and orthorhombic

---

Abbreviations: CZTS, Copper Zinc Tin Sulfide; DMSO, Dimethyl Sulfoxide; XRD, X-Ray Diffractometry; FESEM, Field Emission Scanning Electron Microscopy; UV-Vis NIR, Ultraviolet-Visible Near Infrared; EDS, Energy Dispersive X-Ray Spectroscopy; XPS, X-Ray Photoelectron Spectroscopy; CIGS, Copper Indium Gallium Sulfide; CdTe, Cadmium Telluride; SILAR, Successive Ionic Layer Adsorption and Reaction; CBD, Chemical Bath Deposition; ALD, Atomic Layer Deposition; PCE, Power Coversion Efficiency; CIS, Copper Indium Sulfide; SLG, Soda Lime Glass; PTFE, Poly Tetra-fluoro Ethylene; CCD, Charge Coupled Device; FWHM, Full Width at Half Maximum.

* Corresponding author.

E-mail address: aksengupta@cuet.ac.bd (A.K. Sen Gupta).

https://doi.org/10.1016/j.apsadv.2022.100352
Received 15 August 2022; Received in revised form 20 November 2022; Accepted 28 November 2022

Cu_3SnS_4 at 291 cm^{-1} in the Mg-doped sample. From the EDS results, it appears that 45% of the Zn atoms in both the Cd-doped and Mg-doped samples are partially substituted by Cd and Mg, respectively. The optical band gap for Cd-doped samples decreases from 1.61 eV to 1.56 eV when compared to undoped samples. For Mg-doped samples, the optical band gap shrinks even more to 1.1 eV. This corresponds to shifting of absorbance spectra to higher wavelengths known as "redshift". Urbach energy is determined to be 284 meV and 1072 meV for Cd and Mg doped samples, respectively, to address band tailing issues. Mg doping enhances crystallite size slightly while decreasing microstrain and dislocation density. The RMS surface roughness of Cd and Mg doped samples is 147 nm and 280 nm, respectively. Nevertheless, the primary peaks of Cu, Zn, Sn, S, Cd, Mg, and O, as well as the secondary photoelectron emission lines of these elements, are all found to be present and identified in both the doped samples. These results imply that Cd and Mg doping in the Zn-cationic site of virgin CZTS thin film can be regulated systematically to get appreciated features as a solar cell absorber.

Introduction

Since its inception in 1988 [1], advances in CZTS thin film research have remained a topic of great interest due to a number of promising qualities. They consist of non-toxic and earth-abundant materials, e.g., copper, zinc, tin, and sulfur, with a quaternary tetrahedral crystal structure, a high absorption coefficient over 10^4 cm^{-1}, and tunable optical and morphological features [2]. CZTS thin film is a compound semiconductor composed of three cations and one anion. Various attempts were made to alter both the cationic and anionic sites of the CZTS thin film to improve its performance [3]. The typical optical band gap of pure sulfide CZTS is 1.5 eV. It is possible to modify the optical band gap by introducing Se into the anionic site and changing the ratio of S/(S+Se); 1.0 eV for CZTSe and 1.0 eV~1.5 eV for CZT(S, Se) [4]. To date, CZT(S,Se)-based solar cells have achieved the highest power conversion efficiency (PCE) of 13.0% [5]. However, there are some advantages to use pure sulfide CZTS as an absorber in the solar cell. For instance, selenium is naturally toxic, and the optical band gap of CZTS is identical to that of the solar spectrum [6].

Despite being successfully fabricated, the CZTS thin film solar cell is still unable to compete with other commercially available thin film solar cells like CIGS(Se) and CdTe [7]. Designing an efficient solar cell requires tailoring of the optical band gap and morphological features by passivating crystal imperfections inside the CZTS absorber [8]. The functional relationship among the structural, morphological, and optoelectronic properties of CZTS thin films is significantly altered by the fabrication process, dopants at the film level, and interfacing layers when applied to devices [9].

The methods of fabrication can play critical and vital roles in achieving highly competent qualities in fabricated thin films [10]. CZTS and its derivative thin film fabrication can be divided into two categories: vacuum and non-vacuum. Sputtering, thermal evaporation, and atomic layer deposition (ALD) are vacuum-based techniques [11]. Sol-gel spin coating, spray pyrolysis, successive ionic layer adsorption and reaction (SILAR), doctor blading, the hot injection method, and chemical bath deposition (CBD) are non-vacuum fabrication techniques that rely mostly on chemical synthesis [12–14]. The sol-gel method has a number of advantages over other methods, including superior homogeneity, controllable stoichiometry, great purity, the ability to produce phase-solid powders at a relatively lower temperature, and the flexibility of producing dense monoliths, thin films, or nanoparticles [15–19]. Other potential benefits include very efficient, quick, and straightforward approaches to the production of thin films. While non-vacuum procedures are simpler and less expensive, the management of chemical hazards during synthesis and disposal is a major concern. For instance, there is a report on CZT(S,Se) based solar cell that exhibits a power conversion efficiency (PCE) of 12.6 % which uses hydrazine, a highly hazardous chemical [20]. As a result, selecting a chemical synthesis pathway and employing eco-friendly, non-hazardous chemicals could be a prudent decision in the fabrication process.

Copper, zinc, and tin can be mixed with thiourea in a dimethyl sulfoxide (DMSO) solvent to make a solution of molecular complexes of precursors [21]. A DMSO molecular ink route has many advantages over other ways of processing in the solution phase. It is much safer than using hydrazine ink, and it takes less time to make than using nanocrystal ink. It also gives a unique way to easily add dopants and precisely control the stoichiometry of the absorber [22]. It is also said that adding the precursors to the DMSO solvent in a step-by-step order to get the redox-equilibrated precursor solution leads to better-quality CZTS and higher efficiency [21]. Processing from DMSO solutions, on the other hand, has some issues, like a rough surface and a lack of crystallinity, which affect the performance of the device [23].

Studies reported that off-stoichiometric CZTS outperformed stoichiometric CZTS in photovoltaic performance [24]. Cu_2ZnSnS_4 (CZTS), $Cu_2ZnSnSe_4$ (CZTSe), and $Cu_2ZnSn(S,Se)_4$ (CZTSSe) are multinary compounds that can be produced in various non-stoichiometric compositions, preferably in the Cu-poor, Zn-rich regime. Although, due to this off-stoichiometric composition, there is the possibility to form various detrimental binary and ternary secondary phases along with the CZTS phase. Numerous combinatorial investigations have been conducted since Katagiri's pioneering research in 2005 [25]. However, simply modifying the absorber stoichiometry is not sufficient to increase device performance to a level that is comparable to other thin film solar cells [3]. Thus, the addition of extrinsic atoms in varying amounts to the kesterite-type crystal matrix is being studied to improve the beneficial properties of absorbers [3].

The CZTS compound may develop a variety of intrinsic defects and defect clusters, including vacancies, antisites, and interstrials [8]. The Cu vacancy (V_{Cu}) is the predominant p-type acceptor for ternary compounds like CIS. As CZTS is fabricated as an off-stoichiometric Cu-poor Zn-rich material, it has previously been believed that V_{Cu} is likewise the predominant p-type acceptor defect in CZTS [26]. However, the valence difference between Cu(I) and Zn(II) in the copper-zinc antisite (Cu_{Zn}) in the quaternary complex CZTS is one, making it identical to V_{Cu} [27]. Cu_{Zn} may thus be a strong contender for the dominant p-type acceptor. This Cu_{Zn} may form easily and is more dominant than V_{Cu} because of the lower formation energy. Because of this antisite, carrier recombination centers are made that are dominated by defect states. This lowers the efficiency of the device's power conversion by lowering the open-circuit voltage (V_{OC}).

Therefore, one way to decrease the V_{OC} deficit is to partially replace Zn atoms with an extrinsically doped other atoms during the fabrication of CZTS thin films. This will reduce the density of defects associated with the Cu_{Zn} antisite. To minimize Cu_{Zn} antisite defects, the Cu-cationic site can also be substituted; however, in this article, we will concentrate on the Zn-cationic site. In selecting the dopant atoms for Zn-cationic sites, the size of the atom and its location in the periodic table are important. The band gaps in compound semiconductors get smaller when heavier atoms from the same group in the periodic table are substituted [28]. The atoms having the same isoelectronic configuration as Zn, same valence electrons as Zn, and a larger atomic size than Zn are considered during the dopant selection [29].

In the same group II-B as Zn, Cd is regarded as a potential dopant for a probable partial Zn-cation substitution in the CZTS crystal. Since Cd and Zn atoms have the same electron structure, they are isoelectronic. The atomic radii of Zn and Cd, according to Slater [30], are 1.35Å and

1.55Å, respectively. Therefore, Cd atom is bigger than Zn atom. In addition, the Zn^{2+} and Cd^{2+} ions' respective ionic radii in tetrahedral coordination are 0.6Å and 0.78Å, respectively. It has been discovered that Cd doping for partial Zn cation substitution helps reduce defects brought on by Cu_{Zn}, which lowers the V_{OC} deficit. Initial research on the electronic structure of Cd-doped CZTS and CZTSSe was conducted by Maeda et al. [31]. Rondiya et al. [32] studied the effects of replacing Cd^{2+} in Zn^{2+} lattice sites in CZTS nanocrystals by a solution-based technique and observed a decrease in the optical band gap from 1.51 eV to 1.1 eV. In a different investigation, novel cadmium surface diffusion doping in CZTSSe [33] improved crystal quality, reduced charge density in depletion layers, inhibited the growth of surface secondary phases, and increased power conversion efficiency. The Cd/(Zn+Cd) ratio of 0.4, found to be optimal, was adopted in a report [34] with more than 11% efficient Cd-doped CZTS thin film solar cell. Toxic Cd doping in non-toxic CZTS, might, however, cause additional issues that can exceed the advantages. Taking this into account, the aim behind this present study, to reduce the Cd content by introducing another dopant atom at the same Zn-cationic site in such a way to get same benefit as Cd-dopant alone. In order to fulfill this aim, it is important to study the effects of dopants individually first, and it is the scope of this present article.

As a possible second dopant, we have selected Mg as a non-toxic counterpart of Cd, which is a group II-A element having 1.50Å atomic radius [30], 0.57Å ionic radius, and same valence electrons as Zn atoms. In a work, Wang et al. [35] doped magnesium atoms into CZTS using a DMF-based solution technique, resulting in better electronic, microstructural, and power conversion efficiency. At 20% Mg doping, low-cost sol-gel spin coating was used to get the best electrical and morphological performances in CZTS films [36].

Despite having a handful of reports on individual doping of Cd and Mg in Zn sites for CZTS thin film, there is no study comparing the structural, morphological, electrical, and optical properties between these two dopants in CZTS thin film under similar experimental conditions. In this study, the effects of Cd and Mg doping with a preferable partial substitution of Zn atoms on a pure CZTS thin film were investigated. The sol-gel spin coating method was used for thin film fabrication. The precursors were dissolved in non-toxic DMSO solvent to make the sol-gel before spin coating on the glass substrate. The structural, morphological, and optical properties are analyzed and compared between Cd and Mg-doped CZTS thin film samples.

Material and methods

Corning® soda lime glasses (SLGs) with the dimensions 50 × 50 × 1.2 mm^3 were used as a substrate for all thin film depositions. SLGs were ultrasonically cleaned with sequential immersion into methanol, acetone, methanol again, and deionized water (DI water) for 15 min each before the fabrication began. After that, SLGs were dried with N_2 jet blowing and baked on a hotplate at 120°C.

All reagents and chemicals were purchased from Alfa Aesar, USA of analytical grade and used without further purification. The CZTS sols were made by adding 1.14M copper acetate monohydrate ($Cu(CH_3COO)_2.H_2O$, 99%), 0.79M stannous chloride dihydrate ($SnCl_2.2H_2O$, 98%), 0.82M anhydrous zinc chloride ($ZnCl_2$, 98%), and 4.1M thiourea (CH_4N_2S, 99%) into 50ml dimethyl sulfoxide (DMSO) at room temperature as described in [22]. For doped CZTS samples, the precursors cadmium chloride monohydrate ($CdCl_2.H_2O$) and magnesium chloride hexahydrate ($MgCl_2.6H_2O$) were used in preparing cadmium and magnesium doped sols, respectively. Both the dopants were at 50 mol% relative to $ZnCl_2$ precursor in the sols. The undoped, Cd-doped, and Mg-doped samples are coded as C-00, C-Cd, and C-Mg, respectively. The sols were aged for 72 h and kept in a dark place before the spin coating process started.

The aged sols were filtered with a 0.22 µm PTFE syringe filter (corning®, USA) before coating. We used POLOS SPIN 150i (SPS Europe B.V., The Netherlands) spin coater for thin film fabrication on SLG substrates. Firstly, the SLG substrate is placed on the chuck of the spin coater and 'ON' the vacuum switch so that the substrate is attached firmly. Secondly, 750 µl of sols was pipetted and dropped carefully at the center of the substrate to ensure homogeneous distribution. Thirdly, the spin coating process was started at a spin speed of 1500 rpm for 60 s and then immediately annealed on a hotplate (set at 320°C) for 1 min, followed by natural cooling for another 2 min. This process was repeated five times. The procedure was the same to fabricate for all three batches of samples.

The as-deposited CZTS films were then annealed with 100 mg S pallets inside a graphite box in a tube furnace (GSL-1100X, MTI corporation, USA). The tube furnace was purged with N_2 gas and then evacuated to a base pressure of 300 mTorr. The annealing profile used a ramp rate of 20°C per min to reach a peak temperature of 550°C, where it remained for 30 min before being allowed to cool naturally. Then, samples were soaked in DI water for 20 min to remove any unwanted secondary phases in the films [2]. Soaked samples were then subjected to N_2 gas blowing followed by hot plate drying. Finally, samples were cut by a diamond cutter to different sizes as per requirements for the different characterizations.

The films' average thickness was determined using the cross-sectional images obtained from the FESEM (Zeiss Neon 40 EsB, Wetzlar, Germany). The morphology and surface roughness of the films were investigated using FESEM and 3D profilometer (Filmetrics, San Diego, CA, USA) respectively. Using a Bruker D8 advanced (Bruker

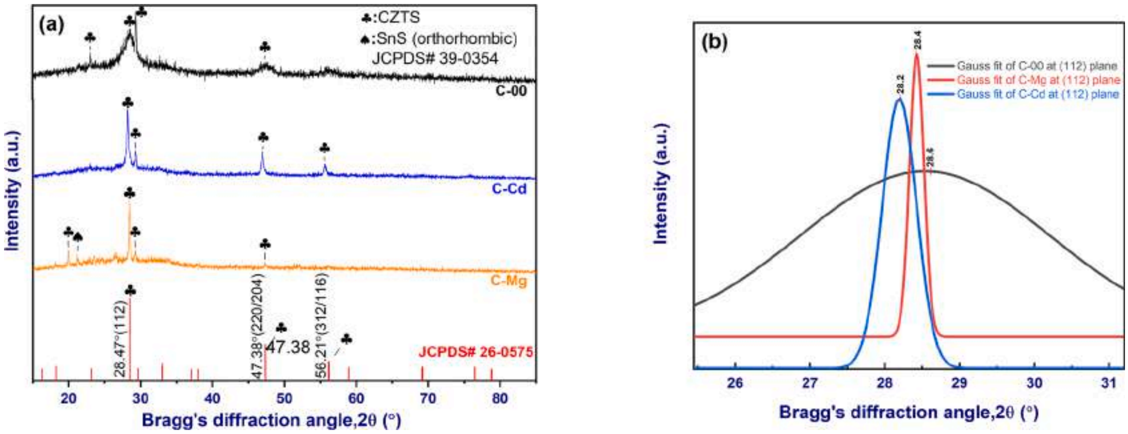

Fig. 1. (a) Bragg's diffraction peaks of sulfurized CZTS thin films as obtained from XRD characterization deposited by sol-gel spin coating method for undoped (C-00), Cd-doped (C-Cd), and Mg-doped (C-Mg) samples (b) an enlarged view of the peak shift around the main diffraction plane (112) after Gauss fitting.

Table 1
Estimation of crystallite size (D), micro strain (ε) and, dislocation density (δ) from XRD data at the preferred orientation plane (112).

Sample	$2\theta_{112}$ (°)	d_{112} (Å)	FWHM (°)	D (nm)	ε ($\times 10^{-3}$)	δ ($\times 10^{11}$ cm^{-2})
C-00	28.6	3.12	2.376	3.45	40.67	83.99
C-Cd	28.2	3.16	0.328	24.94	5.70	1.61
C-Mg	28.4	3.14	0.217	37.69	3.75	0.70

Corporation, Billerica, MA, USA) X-ray diffractometer equipped with Cu Kα radiation, XRD measurements were taken in the range of 10°-90° over the 2θ angle range. Rietveld refinement was performed on the XRD data obtained from the samples, and the results were analyzed with the bulk kesterite model in space group I42m. FullProf suite was used to make the necessary adjustments. The Renishaw spectrometer (in Via Raman Microscope, UK) fitted with a charge-coupled device (CCD) detector was used to carry out the Raman measurements. For excitation, a diode-pumped solid-state laser with a wavelength of 785 nm was utilized. Morphology and chemical composition analysis (Energy dispersive X-ray spectroscopy, EDS) was carried out using FESEM and Thermofisher Quattro S ESEM (Thermo Fisher Scientific Inc., Waltham, MA, USA). EDS was carried out with a total acquisition time of approximately 29 s. The average count rate and acceleration voltage were16011 cps and 15 kV, respectively. The SHIMADZU UV-2600, UV-Vis NIR spectrophotometer (Country of origin: Japan) was used to explore the optical properties over an optical wavelength range of 200 nm to 1400 nm. For pH measurements, pH-indicator strips (non-bleeding, 0-14) MColorpHast^{TM} (Merck KGaA, Dramstadt,Germany) were used. Dynamic viscosity of the prepared solutions was measured by Fungilab RT500 (Bercelona, Spain).

In order to quantify the binding energies and oxidation states of the CZTS thin films, XPS experiments were carried out with a conventional Mg Kα X-ray source (exciting photon energy 1253.6 eV). Following the execution of a Shirley-type background subtraction, the XPS spectra were fitted using Gaussian peak forms.

Results and discussion

Structural properties

X-ray diffraction and Raman characterization were carried out to evaluate the effect of dopants on the structural properties of CZTS absorbers.

The XRD patterns of sulfurized CZTS thin films that were produced from precursor solutions with undoped and doped contents are shown in Fig. 1(a). Although a dominant diffraction peak at the (112) plane is common in all the sulfurized samples, the C-Cd sample exhibits three narrow and strong diffraction peaks from the (112), (220), and (312) planes. All are consistent with the kesterite structure (JCPDS# 26-0575) as reported in [37–39]. At a Bragg's diffraction angle of 21.18°, orthorhombic SnS phase is detected in a C-Mg sample (JCPDS# 39 0354). Other polycrystalline CZTS phase characteristic peaks that correspond to JCPDS# 26-0575 are also indexed.

Fig. 1(b) shows an enlarged view of the peak shift around the main diffraction plane (112) after Gauss fitting of the samples under investigation.

The average crystallite size (D) using the Scherrer formula [40], the microstrain (ε) [41], and the dislocation density (δ) [42] of the deposited films of the principal diffraction peak at the (112) plane were determined as given by Eqs. (1)–(3) and shown in Table 1.

$$D = 0.94\lambda/\beta\cos\theta \tag{1}$$

$$\varepsilon = \beta/4\tan\theta \tag{2}$$

$$\delta = n/D^2 \tag{3}$$

Table 2
Rietveld refinement parameters with lattice constants.

Sample	χ^2	R_F (%)	a = b (Å)	c (Å)	c/2a	Volume (Å)^3
C-00	1.94	10.9	5.424	10.712	0.99	315.16
C-Cd	1.92	10.7	5.467	10.990	1.00	328.45
C-Mg	1.94	9.39	5.426	10.925	1.00	321.70

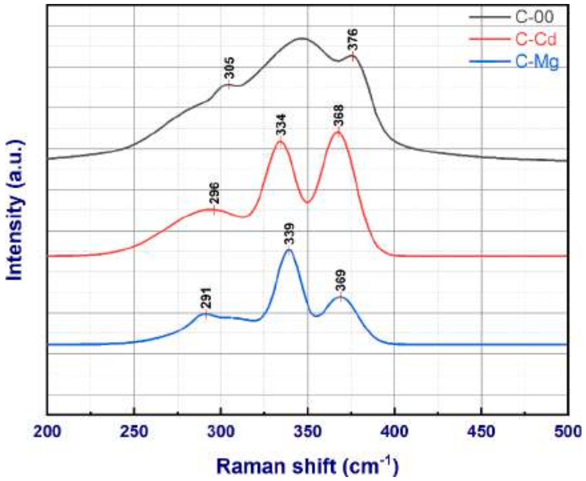

Fig. 2. Raman spectra of sulfurized undoped (C-00), Cd-doped (C-Cd), and Mg-doped (C-Mg) thin film samples.

where,
λ = X-ray wavelength, 1.540056Å
β = Full-width at half-maximum
θ = Half of the Bragg's diffraction angle
n=1.

The Rietveld refinement method is a useful process for extracting crystal structure information from XRD data. Hence, Rietveld refinement was conducted on the XRD data for all of the samples (C-00, C-Cd, and C-Mg) that fell within the 2θ range. The refinement process was carried on until the optimal value for the goodness of fit (χ2) could be determined. In this particular instance, the space group was determined to be I42m, and the peak shape function was decided upon as being pseudo voigt. The refined parameters can be found in Table 2.

Improved crystallite sizes followed by corresponding improvements in microstrain and dislocation densities are found in doped cases, as shown in Table 1.

The main diffraction peak along the (112) plane occurs at $2\theta_{112}$=28.6° in the C-00 sample. The left shift of main diffraction peak at $2\theta_{112}$ = 28.2° for C-Cd sample and $2\theta_{112}$ = 28.4° for C-Mg sample with corresponding increase in interplanar spacing "d", indicates that both samples are subjected to tensile stress. Accordingly, cell volume also increased. This peak shift is due to the variation in the effective ionic radii of Cd^{2+}, Mg^{2+}, and Zn^{2+} ions [43]. When Cd and Mg doped samples are compared to undoped samples, the lattice constants "a" and "c" clearly increase. The observed increase in lattice constant with dopants implies the substitution of Cd and Mg ions for Zn ions without affecting the kesterite structure. As $c/2a \leq 1$ for the doped samples, it confirms the persistence of kesterite crystal structure after doping [29]. The crystallite sizes behaved similarly. The hydrolysis reaction of the metal ions [37] could be one of the reasons for this increase in crystallite size of the doped CZTS, and the samples could have minor structural imperfections [44]. The associated increase in crystallite size may also be attributed to the lattice expansion caused by distortions around the dopant atoms as a result of the mismatch between ionic radii [45]. When comparing the average crystallite size of the C-Cd and C-Mg samples, the lower value for the C-Cd sample may be attributed to disturbance in the

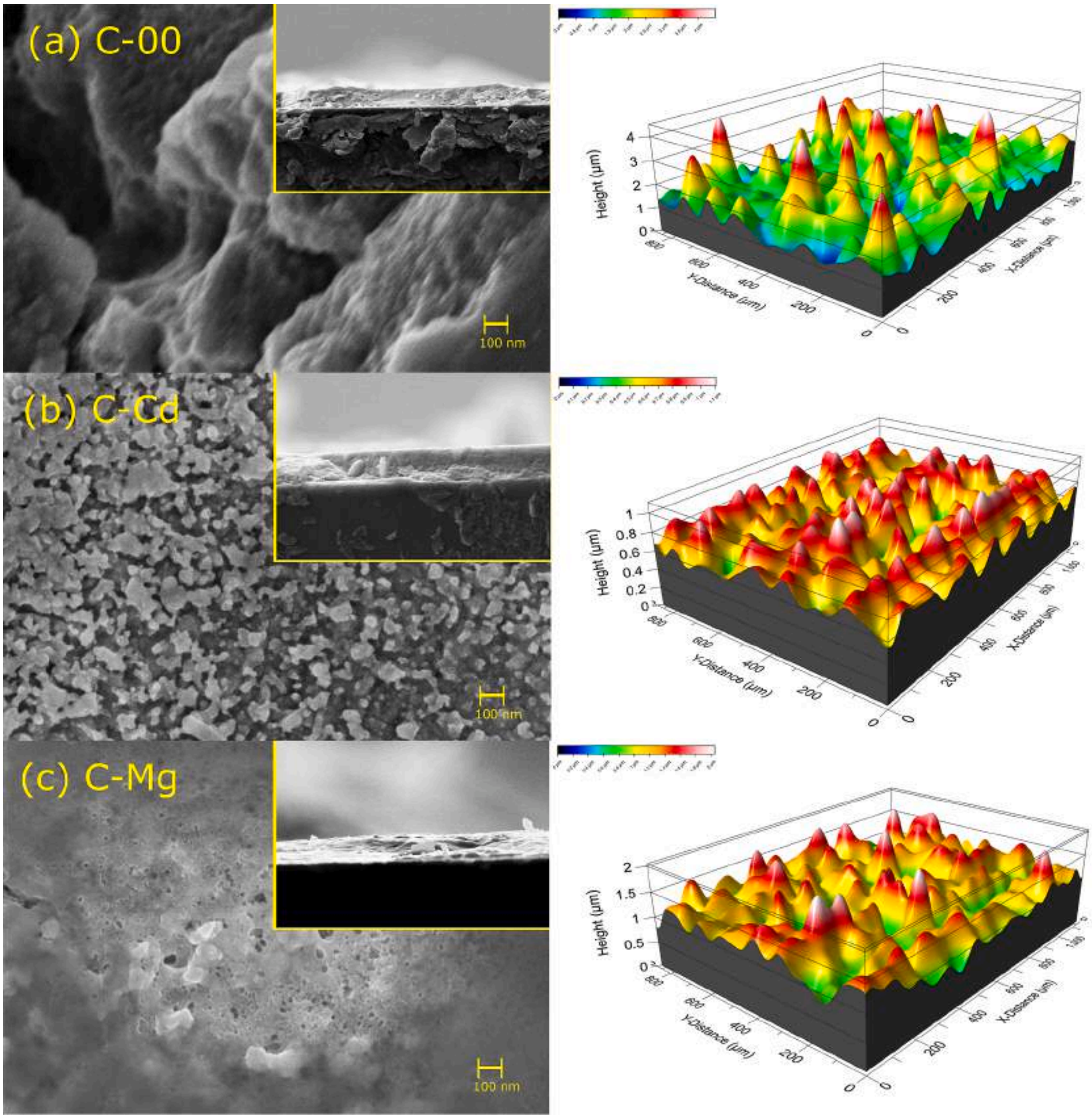

Fig. 3. Typical top-view FESEM images (cross-sectional views at inset) and 3D profilometric surface roughness of CZTS thin films prepared from sol-gel spin coating method: (a) undoped sample (C-00), (b) Cd-doped sample (C-Cd), and (c) Mg-doped sample (C-Mg).

host crystal lattice, which suppresses crystal growth, as supported by the work reported at [45].

The microstrain and dislocation density confirm the considerable deviation in the structural imperfections [46]. In our study, the behavior of the dislocation density and the microstrain is not identical; rather, their behavior varies depending on the dopants and is minimally suffered by the Mg-doped sample. Deterioration of crystalline quality suggests the highest lattice dislocation levels in the undoped C-00 sample.

There is a possibility that some secondary phases, such as tetragonal Cu_2SnS_3, will occur in the same diffraction angle, resulting in an overlapped peak at the (112) plane [47]. However, XRD studies alone cannot confirm the presence of a secondary phase along with kesterite CZTS. Therefore, Raman spectroscopy with an excitation wavelength of 785 nm was utilized to identify possible secondary phases on the undoped and doped CZTS thin films, as shown in Fig. 2.

The main Raman peak, which corresponds to the primary vibrational A1 symmetry mode of single-phase CZTS with a kesterite structure, occurs at 338 cm^{-1} [48]. This particular A1 phonon mode is connected to the vibration of sulfur atoms that are surrounded by atoms from other molecules. However, the undoped C-00 sample does not exhibit this primary CZTS peak, which is a sign that the film is weakly crystalline. A shoulder peak at 376 cm^{-1} corresponds to the characteristic of kesterite structure at mode E/B-TO LO [49,50] is also detected in the C-00 sample. This peak is detected at 368 cm^{-1} in the C-Cd sample and at 369 cm^{-1} in the C-Mg sample, respectively.

The Cu_2CdSnS_4 compound's A1 mode position at 326 cm^{-1} has previously been reported [29]. In this sense, the A1 mode of the Cd-doped sample has peak positions between 338 cm^{-1} and 326 cm^{-1} depending on the Cd concentrations in the film. When doping a C-Cd sample, some of the Zn^{2+} ions are replaced by the larger Cd^{2+} ions. In our study, the A1 mode main Raman peak moved to a lower wavenumber at 334 cm^{-1} upon cadmium doping, which is called a "redshift," while subsequent increases in Cd concentration did not affect the frequency of the main A1 mode.

When 60% of the Zn^{2+} ions were replaced with Mg^{2+} ions, the redshift of the A1 mode peak was discovered to be at 333 cm^{-1} [36]. This shifting was discovered at 335 cm^{-1} for 5% Zn^{2+} ion replacement in another study [35]. In our investigation, magnesium doping with 45% Zn^{2+} ion replacement results in the detection of the A1 mode primary Raman signal at 339 cm^{-1}. It could be a possibility for lattice flaws to cause dislocations that alter the distribution of lattice constants [51].

Table 3
Surface roughness data from 3D profilometry.

Parameters*	C-00 (μm)	C-Cd (μm)	C-Mg (μm)
S_p (Peak height,μm)	2.885	0.392	0.939
S_v (Valley height,μm)	1.178	0.531	1.020
S_t (Maximum peak-to valley height,μm)	4.063	0.923	1.960
S_a (Arithmetic mean height,μm)	0.455	0.116	0.215
S_q (Root mean square height,μm)	0.615	0.147	0.280

[*] Area (Width = 564.4 μm; Height = 421.6 μm) roughness

According to Fig. 1(a), one of the distinctive kesterite peaks for the C-Mg sample is not present along the (312) plane, and a new characteristic peak is identified at 23.18°. Additionally, while lattice constant "a" remains almost constant, the change in lattice constant "c" impacts the rise in cell volume (Table 2).

In three samples, three Cu-Sn-S (CTS) related secondary phases with different crystal structures have been identified. Cubic Cu_2SnS_3 phase at 305 cm^{-1} [52] in C-00, tetragonal Cu_2SnS_3 phase at 296 cm^{-1} [53] in C-Cd, and orthorhombic Cu_3SnS_4 at 291 cm^{-1} [52,54] in the C-Mg sample.

Morphological properties

The impact of doping on the morphology and surface roughness of the films were investigated using FESEM and a 3D profilometer, respectively. SEM micrographs, and surface roughness of the deposited thin films are shown in Fig. 3.

The scanning electron microscopy images showed that the Cd-doped sample had grains that were closely packed together, which were not observed in the Mg-doped or undoped samples. The reported variations in crystallite size are consistent with SEM findings.

Thin films with high crystalline quality are made by choosing the right chemical precursors, type of solvent, and other factors that control solution parameters like pH and viscosity [51]. The pH of all precursor solutions prepared for thin film fabrication using the sol-gel spin coating technique was about 5.5. The centipoise (cp) is a measurement unit for dynamic viscosity. For the sample C-00, C-Cd, and C-Mg solutions, the observed values for dynamic viscosity (room temperature = 28°C) were 22.6 cp, 22.0 cp, and 23.8 cp, respectively. As a result, the C-Mg sample was found to be more adherent to the SLG glass substrate, which was attributed to better crystallinity.

According to the three-dimensional profilometry results (Table 3), both doped samples had lower root mean square (RMS) heights than the

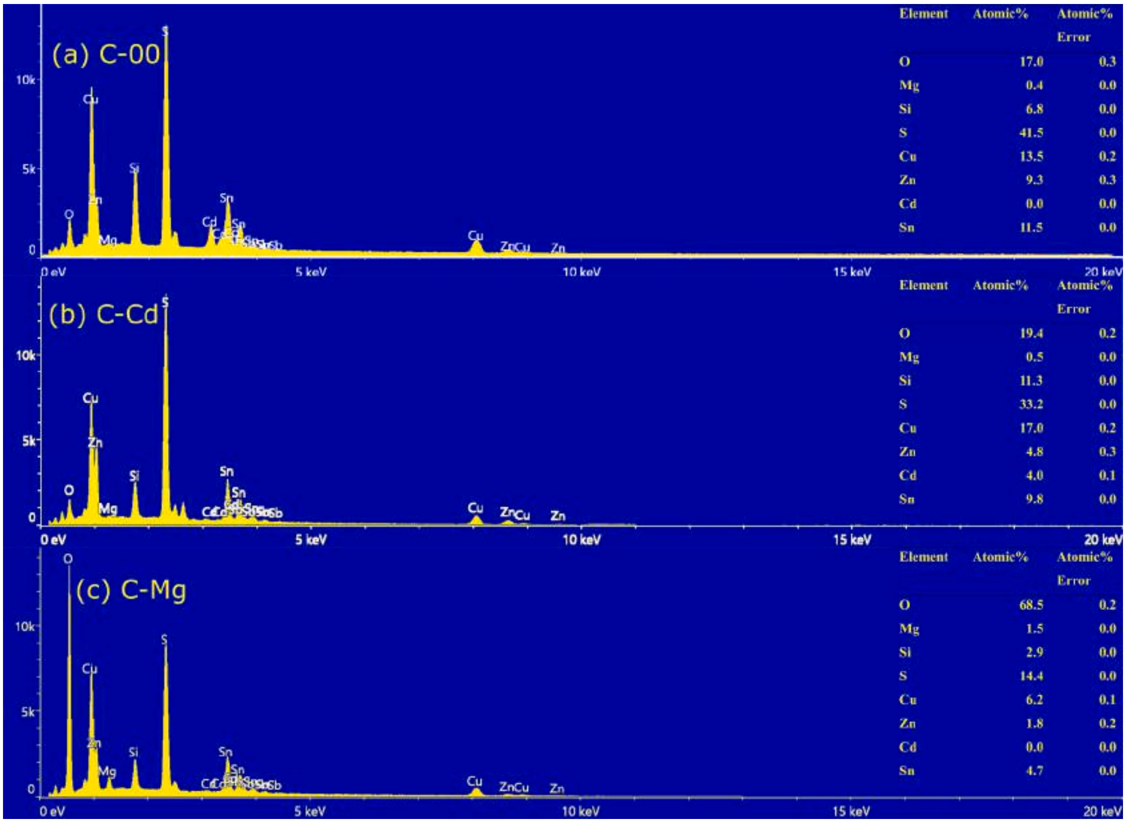

(a)

Element	Atomic%	Atomic% Error
O	17.0	0.3
Mg	0.4	0.0
Si	6.8	0.0
S	41.5	0.0
Cu	13.5	0.2
Zn	9.3	0.3
Cd	0.0	0.0
Sn	11.5	0.0

(b)

Element	Atomic%	Atomic% Error
O	19.4	0.2
Mg	0.5	0.0
Si	11.3	0.0
S	33.2	0.0
Cu	17.0	0.2
Zn	4.8	0.3
Cd	4.0	0.1
Sn	9.8	0.0

(c)

Element	Atomic%	Atomic% Error
O	68.5	0.2
Mg	1.5	0.0
Si	2.9	0.0
S	14.4	0.0
Cu	6.2	0.1
Zn	1.8	0.2
Cd	0.0	0.0
Sn	4.7	0.0

Fig. 4. EDS spectrum of sulfurized thin film samples: (a) undoped (C-00), (b) Cd-doped (C-Cd), and (c) Mg-doped (C-Mg).

Table 4
Doping and the elemental composition ratio of sulfurized samples as obtained by EDS.

Sample code	Doping ratio in the sulfurized thin films		Active composition ratio in the sulfurized thin films		
	For Cadmium, $Cu_2Zn_{(1-x)}Cd_xSnS_4$	For Magnesium, $Cu_2Zn_{(1-y)}Mg_ySnS_4$			
	$x = \frac{Cd}{Cd + Zn}$	$y = \frac{Mg}{Mg + Zn}$	$\frac{Cu}{Zn + (Cd + Mg) + Sn}$	$\frac{Zn + (Cd + Mg)}{Sn}$	$\frac{S}{Cu + Zn + (Cd + Mg) + Sn}$
C-00	0.00	0.04	0.64	0.84	1.19
C-Cd	0.45	0.09	0.89	0.95	0.92
C-Mg	0.00	0.45	0.78	0.70	1.01

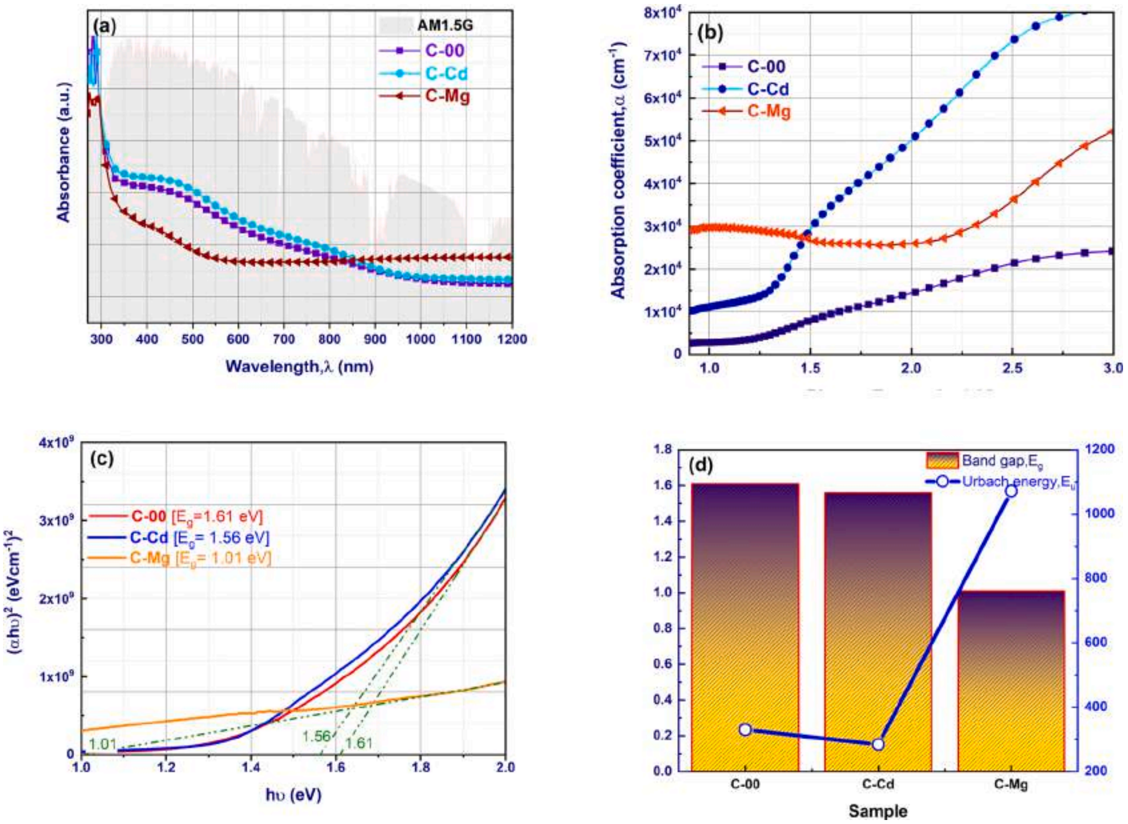

Fig. 5. Optical properties CZTS thin films prepared from sol-gel spin coating method with undoped and doped samples: (a) UV–VIS NIR absorbance spectra with AM1.5G solar spectrum (data adopted from NREL website) at background, (b) absorption coefficients vs incident photon energy, (c) Tauc's plots for optical band gap estimations, and (d) variations of optical band gaps with Urbach energies.

undoped sample, with the Cd-doped sample having the lowest value, around 147 nm.

EDS was also utilized in conjunction with SEM analyses to estimate the elemental composition ratio of the elements in the deposited thin films. Fig. 4 depicts the at% of the elements as determined by EDS measurements. The doping and elemental composition ratios of sulfurized samples as obtained by EDS are shown in Table 4. The off-stoichiometric Cu-poor, Zn-rich ratio was seen in all of the fabricated thin films. A similar observation was also reported in [24]. It appears that 45% of the zinc atoms in both the C-Cd ($CZn_{0.55}Cd_{0.45}TS$) and C-Mg ($CZn_{0.55}Mg_{0.45}TS$) samples are partially substituted by cadmium and magnesium atoms, respectively. Some of the Mg in sample C-00, which has not been doped, could come from the soda lime glass substrate.

It can be seen that XRD peak intensities change a lot depending on the active composition ratio of the Cu/(Zn+Cd+Mg+Sn) stoichiometry (Table 4). When this ratio is 0.89 for a C-Cd sample, the XRD peak intensity is the highest. It gradually decreases when this ratio is 0.78 for a C-Mg sample and 0.64 for a C-00 sample.

Taking into account the foregoing, we might conjecture as to what prompted the doped thin films' morphological change. Films created on a glass substrate were neither tightly packed nor homogenous, despite the fact that Mg-doped samples were formed in a more crystalline manner than Cd-doped samples, resulting in marginally higher crystallite sizes. Mg-doped sample also had the highest RMS surface roughness as a result. In SEM images of the Mg-doped sample, the grain boundaries are challenging to figure out. Sn amounts on the surface, may influence the morphology changes when Cd and Mg dopants are introduced. When comparing the C-Cd and C-Mg samples, EDS and XPS reveal that the C-Cd sample has a more Sn-rich surface.

Optical properties

Before investigating the optical properties of fabricated thin films, the thickness of the samples was measured using cross-sectional SEM observations. The samples C-00, C-Cd, and C-Mg each had a thickness of 2.075 μm, 0.724 μm, and 0.527 μm, respectively.

The absorbance spectra of the CZTS thin films were found and are shown in Fig. 5(a). Fig. 5(b) and Fig. 5(c) show the corresponding absorption coefficients and Tauc's plots.

The optical absorption coefficient, α of a direct band gap semiconductor near the band edge, for photon energy, hυ greater than the band gap energy, E_g of the semiconductor, is given by Tauc's relation [55], as in Eq. (4).

$$\alpha h\nu = A\left(h\nu - E_g\right)^{1/2} \tag{4}$$

where A is a constant, h is Planck's constant, and υ is the frequency of the incident photon. The Tauc's plots of $(\alpha h\nu)^2$ versus incident photon energy, hυ for the undoped and doped samples are plotted. Extrapolating the linear part of the Tauc's plot curves to intercept the energy axis at $(\alpha h\nu)^2 = 0$ yielded the band gap energy.

The absorption coefficients are found to be on the order of 10^4 cm^{-1} for all of the samples. This supports the fact that the material experienced direct transitions from one state to another.

There was a report of a Cu_2CdSnS_4 compound with an optical band gap of 1.38 eV in [56]. So, it was expected that the optical band gap, E_g of the Cd-doped sample would be less than that of the undoped sample. The E_g is estimated to be approximately 1.61 eV in the undoped sample, C-00. This higher value of the optical band gap for an undoped CZTS sample may be due to the presence of defect or trap states within the forbidden energy gap [51]. The band gap was found to fall to 1.56 eV after doping with cadmium.

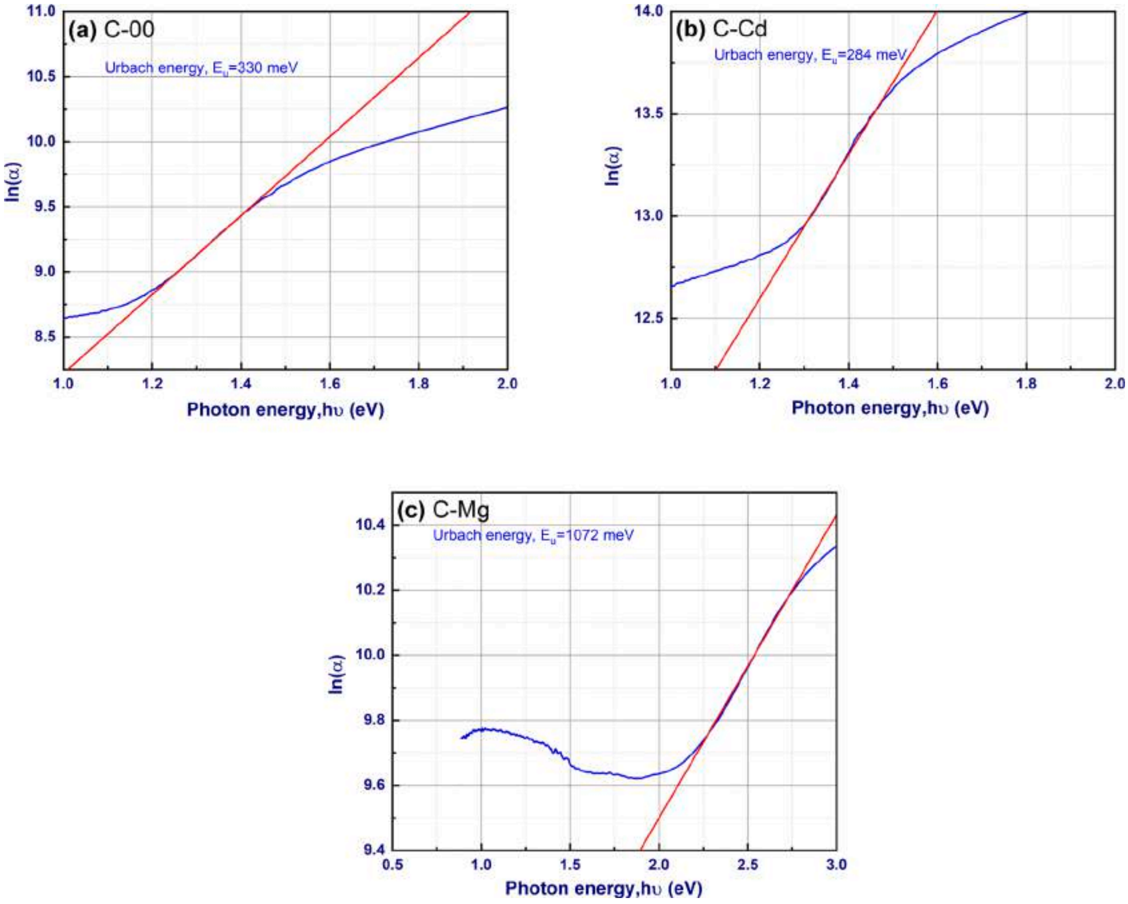

Fig. 6. Urbach energy determination of sulfurized thin film samples: (a) undoped (C-00), (b) Cd-doped (C-Cd), and (c) Mg-doped (C-Mg).

On the other hand, the optical band gap value decreased even further to 1.01 eV for magnesium doping. Similar results were also reported in the previous studies [57–59]. The following arguments can be used to explain why band gaps decreased after doping. Firstly, as shown in Fig. 5 (a), the location of the absorption edge shifts toward higher wavelengths (redshift). As a result of this redshift, the band gap values of the doped thin films decreased from higher to lower energy. This is most likely due to the increase in crystallite size [60] with a corresponding decrease in FWHM and decrease in the defect states [37,61–63] of the C-Cd and C-Mg thin films. Secondly, the band gap energy may also alter owing to p-d hybridization between Cu d-levels and S p-levels along with the impurity phases present in the samples [27,64]. Thirdly, the formation of donor levels below the conduction band [65], as well as the possibility of dopant-related secondary phases [66], may both contribute to the redshift of the optical absorption edge, resulting in a smaller band gap.

In addition, the segregation of the host (undoped) atoms besides the grain boundaries can reduce the E_g of doped thin films [67] which is supported by SEM micrographs (Fig. 3). Fig. 5(a) shows that the absorbance of the C-Cd sample is higher than that of the C-Mg sample. We have already seen that the crystallite size of a C-Cd film is smaller than that of a C-Mg film. Doping increased the optical absorbance because decreasing the size of crystallites can lead to an increase in their specific surface area [60].

Urbach energy, E_u plays a vital part in the process of discovering solutions to band tailing problems associated with structural disorder, phonons, excitons, and contaminants. Urbach's tail refers to the absorption edge that is below the energy gap, which rises exponentially [68]. The E_u of deposited thin films was determined for each sample as illustrated in Fig. 6. The Urbach energy is explained within the context of Einstein's model, and it is possible to condense it into an empirical formula presented by [69] and shown in Eq. (5).

$$\alpha = \alpha_0 \exp(h\nu / E_u) \tag{5}$$

The methods of determining the numerical values of Urbach energy are also well detailed in the literature [70]. The Urbach energies of undoped, cadmium doped, and magnesium doped samples were determined from Fig. 6(a)–(c). In this study, significant band tailing problems were observed for the Mg-doped sample (E_u=1072 meV). Cd-doped sample suffers less band tailing issues with a minimum E_u, 284 meV. These values are consistent with the other characterization results acquired in our experiments. A plot of the variation of optical band gaps as obtained for sulfurized samples (C-00, C-Cd, and C-Mg) with respect to their Urbach energies is shown in Fig. 5(d).

Chemical bonding states

The XPS analysis was performed to find the chemical bonding states in the doped thin film samples. Typical XPS wide-scan survey spectra of C-Cd and C-Mg samples are shown in Fig. 7(a) and Fig. 7(b). The primary peaks of Cu, Zn, Sn, S, Cd, Mg, and O, as well as the secondary photoelectron emission (Auger lines) lines of these elements, were all found to be present and identified. The oxidation states of the component elements were determined by measuring spectra with a high resolution of the elements Cu 2p, Zn 2p, Sn 3d, and S 2p (Fig. 7(c)–(f)). In the Cu 2p spectrum, there were two peaks that appeared at the binding energies of 930.82 eV and 949.51 eV for the C-Cd sample, with a peak splitting energy of 18.69 eV. Furthermore, some satellite peaks were discovered at the higher binding energy position. This indicates that the sample contains more than just Cu(I). On the other hand, the Cu 2p spectrum can be seen for the C-Mg sample when the binding energy is between

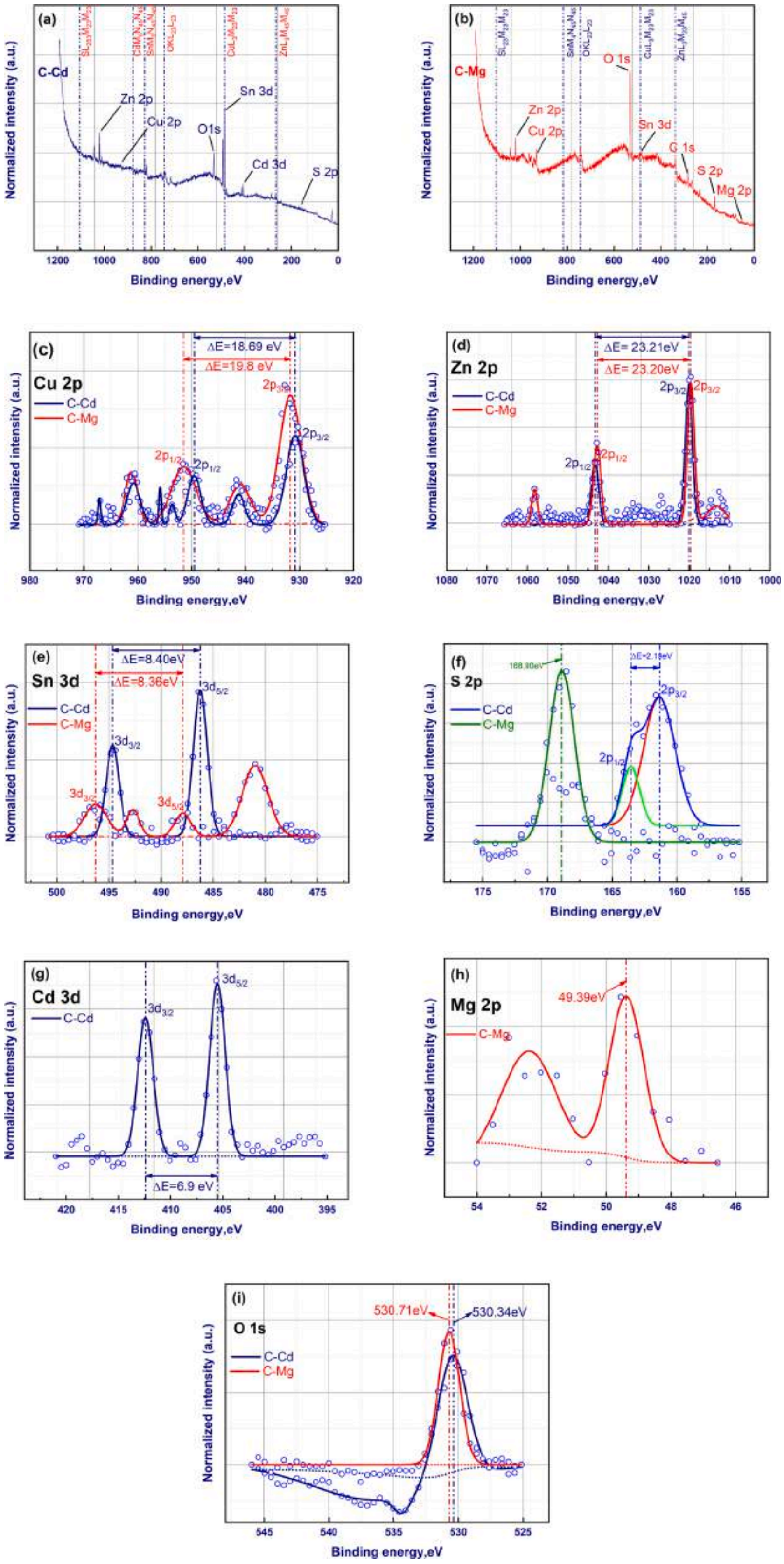

Fig. 7. XPS survey and core level spectra of the CZTS thin films prepared by sol-gel spin coating method with Cd and Mg doping: (a) survey spectra of Cd-doped sample, (b) survey spectra of Mg-doped sample, (c) high resolution Cu 2p core level spectra, (d) high resolution Zn 2p core level spectra, (e) high resolution Sn 3d core level spectra, (f) high resolution S 2p core level spectra, (g) high resolution Cd 3d core level spectra, (h) high resolution Mg 2p core level spectra, and (i) high resolution O 1s core level spectra.

931.7 eV and 951.5 eV, and the peak splitting energy is 19.8 eV. In addition, there were several satellite peaks. When compared to C-Cd, the intensity of Cu 2p in C-Mg is much greater. This observation suggests that the surface contains a comparatively larger concentration of copper. Zn 2p is responsible for the peaks that appear at binding energies of around 1020.10 eV and 1043.31 eV in each of the samples, with a peak separation of 23.20 eV that corresponds to Zn (II). Both samples show Sn (IV) 3d peaks with nearly identical peak splitting energies of 8.4 eV [71]. For the C-Cd sample, which has a more Sn-rich surface than the C-Mg sample, the Sn (IV) 3d peaks are located at 486.25 eV and 494.65 eV. The shifting of Sn (IV) 3d peaks was found at lower binding energy for the CZTSSe sample [72]. However, in this study, the peaks of the Sn 3d core levels shifted towards a higher energy when some satellite peaks appeared in the C-Mg sample. This is in contrast to the shifting that occurred at a higher energy for the C-Mg sample. The peaks of S 2p that arise at binding energies of 161.36 eV and 163.55 eV for the C-Cd sample have matching peak separations of 2.19 eV. This observation indicates that sulfur is present in the sulfide (-II) form. In the case of the C-Mg sample, there is an indication of the existence of the sulfur as sulfate (-II) state in the form of a single peak of S 2p at 168.9 eV. The presence of cadmium is demonstrated by the appearance of two peaks in the Cd 3d spectra (Fig. 7(g)), which are located at the binding energies of 405.51 eV and 412.41 eV for the C-Cd sample. The peak splitting energy is 6.9 eV. A peak in the Mg 2p spectra (Fig. 7(h)) that appears at a binding energy of 49.39 eV provides evidence that magnesium is present in the C-Mg sample. The fact that the intensity of O 1s in C-Mg is higher than that of C-Cd, as shown in Fig. 7(i), implies that there is oxygen contamination on the surface.

Conclusions

The structural, morphological, and optical properties of the undoped, Cd-doped, and Mg-doped CZTS thin films were evaluated, analyzed, and compared. XRD showed the presence of the kesterite phase for undoped and doped samples. Both doped samples exhibited this phase with narrower and stronger diffraction peaks as compared to the undoped sample. The main diffraction peak at the (112) plane shifted towards a lower diffraction angle as referenced to an undoped sample due to the larger ionic radii of dopants . The main A1 mode Raman peak was detected at 334 cm^{-1} and at 339 cm^{-1} in the Cd-doped and the Mg-doped samples, respectively. Because it is poorly crystallized, it cannot be detected in an undoped sample. Distinct Cu-Sn-S (CTS) related secondary phases have been found in three different samples. The C-00 sample had the cubic Cu_2SnS_3 phase at 305 cm^{-1}, the C-Cd sample had the tetragonal Cu_2SnS_3 phase at 296 cm^{-1}, and the C-Mg sample had the orthorhombic Cu_3SnS_4 phase at 291 cm^{-1}. FESEM showed the cadmium doped sample had closely packed grains, which were not observed in the Mg-doped nor in the undoped sample. EDS analysis showed that the off-stoichiometric "active composition ratio" soared in the doped samples, which is suitable for photovoltaic applications. Cd doping suppressed the band tailing issues significantly. The Cd-doped sample is found to have low band tailing issues with a Urbach energy of 284 meV. Its optical band gap was found to be 1.56 eV, which is suitable for photovoltaic applications. Finally, the XPS analysis reconfirmed the presence of dopants in the films and determined the chemical bonding states of the CZTS compound. This study contributes to better understanding the impact of Cd and Mg dopants on the different properties of CZTS thin films. With the knowledge gained from this study, CZTS thin films could be improved and employed as absorbers in thin film solar cells.

CRediT authorship contribution statement

Ashoke Kumar Sen Gupta: Conceptualization, Methodology, Investigation, Writing – original draft. **Syed Farid Uddin Farhad:** Investigation, Resources, Data curation. **Md. Shehan Habib:** Investigation, Resources, Data curation. **Mohammad Robiul Hossan:** Formal analysis, Validation, Writing – review & editing. **Khalid Hossain:** Resources, Data curation. **Nipu Kumar Das:** Resources, Visualization. **Muhammad Quamruzzaman:** Supervision, Writing – review & editing. **M.A. Matin:** Supervision, Writing – review & editing, Funding acquisition. **N. Amin:** Supervision, Project administration.

Declaration of Competing Interest

The authors declare that they have no known competing financial interests or personal relationships that could have appeared to influence the work reported in this paper.

Data Availability

Data will be made available on request.

Acknowledgements

The authors would like to thank the *Renewable Energy Laboratory* at the Department of Electrical and Electronic Engineering, Chittagong University of Engineering and Technology, Chattogram, Bangladesh, which was funded by the World Bank and established by the University Grant Commission (UGC) of Bangladesh as part of the Higher Education Quality Enhancement Project (HEQEP), CP-3200.

References

[1] H. Katagiri, N. Sasaguchi, S. Hando, S. Hoshino, J. Ohashi, T. Yokota, Preparation and evaluation of Cu_2ZnSnS_4 thin films by sulfurization of E-B evaporated precursors, Sol. Energy Mater. Sol. Cells 49 (1–4) (1997) 407–414, https://doi.org/10.1016/S0927-0248(97)00119-0. Dec.
[2] H. Katagiri, et al., Development of CZTS-based thin film solar cells, Thin Solid Films 517 (7) (2009) 2455–2460, https://doi.org/10.1016/j.tsf.2008.11.002. Feb.
[3] Y.E. Romanyuk, et al., Doping and alloying of kesterites, J. Phys. Energy 1 (4) (2019), https://doi.org/10.1088/2515-7655/ab23bc.
[4] M. Dimitrievska, et al., Role of S and Se atoms on the microstructural properties of kesterite $Cu_2ZnSn(S_xSe_{1-x})_4$ thin film solar cells, Phys. Chem. Chem. Phys. 18 (12) (2016) 8692–8700, https://doi.org/10.1039/c5cp07577g. Mar.
[5] "Best Research-Cell Efficiency Chart | Photovoltaic Research | NREL." https://www.nrel.gov/pv/cell-efficiency.html (accessed Dec. 02, 2022).
[6] M.P. Suryawanshi, et al., CZTS based thin film solar cells: a status review, Mater. Technol. 28 (1–2) (2013) 98–109, https://doi.org/10.1179/1753555712Y.0000000038. Mar.
[7] K.K.M. Mamta, V.N. Singh, Comparison of various thin-film-based absorber materials: a viable approach for next-generation solar cells, Coatings 12 (3) (2022) 3, https://doi.org/10.3390/coatings12030405. Mar.
[8] S. Chen, J.H. Yang, X.G. Gong, A. Walsh, S.H. Wei, Intrinsic point defects and complexes in the quaternary kesterite semiconductor Cu_2ZnSnS_4, Phys. Rev. B Condens. Matter Mater. Phys. 81 (24) (2010), 245204, https://doi.org/10.1103/PhysRevB.81.245204. Jun.
[9] T.J. Huang, X. Yin, G. Qi, H. Gong, CZTS-based materials and interfaces and their effects on the performance of thin film solar cells, Phys. Status Solidi Rapid Res. Lett. 8 (9) (2014) 735–762, https://doi.org/10.1002/pssr.201409219. Sep.
[10] S. Goktas, A. Goktas, A comparative study on recent progress in efficient ZnO based nanocomposite and heterojunction photocatalysts: a review, J. Alloys Compd. 863 (2021), 158734, https://doi.org/10.1016/j.jallcom.2021.158734.
[11] Q. Guo, H.W. Hillhouse, R. Agrawal, Synthesis of Cu_2ZnSnS_4 nanocrystal ink and its use for solar cells, J. Am. Chem. Soc. 131 (33) (2009) 11672–11673, https://doi.org/10.1021/ja904981r. Aug.
[12] M.Y. Yeh, P.H. Lei, S.H. Lin, C. Da Yang, Copper-Zinc-Tin-Sulfur thin film using spin-coating technology, Materials (Basel) 9 (7) (2016) 7, https://doi.org/10.3390/ma9070526. Jul.
[13] N.K. Youn, et al., Cu_2ZnSnS_4 solar cells with a single spin-coated absorber layer prepared via a simple sol-gel route, Int. J. Energy Res. 40 (5) (2016) 662–669, https://doi.org/10.1002/er.3446. Apr.
[14] Y. Fang, J.R. Dilworth, M. Pepper, P.P. Edwards, Investigations of the optical and electronic effects of silicon and indium co-doping on ZnO thin films deposited by spray pyrolysis, Z. Naturforsch. - Sect. B J. Chem. Sci. 75 (1–2) (2020) 23–32, https://doi.org/10.1515/znb-2019-0196. Feb.
[15] A. Goktas, A. Tumbul, Z. Aba, M. Durgun, Mg doping levels and annealing temperature induced structural, optical and electrical properties of highly c-axis oriented ZnO:Mg thin films and Al/ZnO:Mg/p-Si/Al heterojunction diode, Thin Solid Films 680 (2019) 20–30, https://doi.org/10.1016/j.tsf.2019.04.024.

[16] A. Tumbul, et al., Solution processed boron doped ZnO thin films: influence of different boron complexes, Mater. Res. Express 6 (3) (2019), https://doi.org/10.1088/2053-1591/aaf4d8.

[17] A. Goktas, F. Aslan, A. Tumbul, S.H. Gunduz, Tuning of structural, optical and dielectric constants by various transition metal doping in ZnO:TM (TM=Mn, Co, Fe) nanostructured thin films: a comparative study, Ceram. Int. 43 (1) (2017) 704–713, https://doi.org/10.1016/j.ceramint.2016.09.217.

[18] A. Goktas, High-quality solution-based Co and Cu co-doped ZnO nanocrystalline thin films: comparison of the effects of air and argon annealing environments, J. Alloys Compd. 735 (2018) 2038–2045, https://doi.org/10.1016/j.jallcom.2017.11.391.

[19] H. Gencer, A. Goktas, M. Gunes, H.I. Mutlu, S. Atalay, Electrical transport and magnetoresistance properties of $La_{0.67}Ca_{0.33}MnO_3$ film coated on Pyrex glass substrate, Int. J. Mod. Phys. B 22 (5) (2008) 497–506, https://doi.org/10.1142/S0217979208038776.

[20] W. Wang, et al., Device characteristics of CZTSSe thin-film solar cells with 12.6% efficiency, Adv. Energy Mater. 4 (7) (2014), https://doi.org/10.1002/aenm.201301465. May.

[21] H. Xin, J.K. Katahara, I.L. Braly, H.W. Hillhouse, 8% Efficient $Cu_2ZnSn(S,Se)_4$ solar cells from redox equilibrated simple precursors in DMSO, Adv. Energy Mater. 4 (11) (2014), https://doi.org/10.1002/aenm.201301823. Aug.

[22] H. Xin, et al., Lithium-doping inverts the nanoscale electric field at the grain boundaries in $Cu_2ZnSn(S,Se)_4$ and increases photovoltaic efficiency, Phys. Chem. Chem. Phys. 17 (37) (2015) 23859–23866, https://doi.org/10.1039/c5cp04707b. Aug.

[23] Y.E. Romanyuk, et al., Recent trends in direct solution coating of kesterite absorber layers in solar cells, Sol. Energy Mater. Sol. Cells 119 (2013) 181–189, https://doi.org/10.1016/j.solmat.2013.06.038.

[24] H. Katagiri, K. Jimbo, M. Tahara, H. Araki, K. Oishi, The influence of the composition ratio on CZTS-based thin film solar cells, MRS Proc. (2009), https://doi.org/10.1557/PROC-1165-M04-01.

[25] H. Katagiri, Cu_2ZnSnS_4 thin film solar cells, Thin Solid Films 480–481 (2005) 426–432, https://doi.org/10.1016/j.tsf.2004.11.024.

[26] J.M. Raulot, C. Domain, J.F. Guillemoles, Ab initio investigation of potential indium and gallium free chalcopyrite compounds for photovoltaic application, J. Phys. Chem. Solids 66 (11) (2005) 2019–2023, https://doi.org/10.1016/j.jpcs.2005.09.097.

[27] S. Chen, X.G. Gong, A. Walsh, S.H. Wei, Defect physics of the kesterite thin-film solar cell absorber Cu_2ZnSnS_4, Appl. Phys. Lett. 96 (2) (2010) 21902, https://doi.org/10.1063/1.3275796. Jan.

[28] Z. Su, J.M.R. Tan, X. Li, X. Zeng, S.K. Batabyal, L.H. Wong, Cation substitution of solution-processed Cu_2ZnSnS_4 thin film solar cell with over 9% efficiency, Adv. Energy Mater. 5 (19) (2015) 2–8, https://doi.org/10.1002/aenm.201500682.

[29] M. Courel, et al., Impact of Cd concentrations on the physical properties of $Cu_2(Cd_xZn_{1-x})SnS_4$ thin films, Superlatt. Microstruct. 122 (2018) 324–335, https://doi.org/10.1016/j.spmi.2018.07.032. Oct.

[30] J.C. Slater, Atomic radii in crystals, J. Chem. Phys. 41 (10) (1964) 3199–3204, https://doi.org/10.1063/1.1725697. Nov.

[31] T. Maeda, S. Nakamura, T. Wada, First-principles study on Cd doping in Cu_2ZnSnS_4 and $Cu_2ZnSnSe_4$, Jpn. J. Appl. Phys. 51 (10 PART 2) (2012) 10NC11, https://doi.org/10.1143/JJAP.51.10NC11/XML. Oct.

[32] S.R. Rondiya, et al., Solution-processed Cd-substituted CZTS nanocrystals for sensitized liquid junction solar cells, J. Alloys Compd. 890 (2022), https://doi.org/10.1016/j.jallcom.2021.161575.

[33] H. Luan, et al., Mechanism of enhanced power conversion efficiency of $Cu_2ZnSn(S,Se)_4$ solar cell by cadmium surface diffusion doping, J. Alloys Compd. 876 (2021), https://doi.org/10.1016/j.jallcom.2021.160160.

[34] T.K. Todorov, et al., Beyond 11% efficiency: characteristics of state-of-the-art $Cu_2ZnSn(S,Se)_4$ solar cells, Adv. Energy Mater. 3 (1) (2013) 34–38, https://doi.org/10.1002/aenm.201200348. Jan.

[35] Y. Wang, et al., Effect of Mg doping on Cu_2ZnSnS_4 solar cells prepared by DMF-based solution method, Opt. Mater. (Amst). 117 (2021), https://doi.org/10.1016/j.optmat.2021.111211. Mar.

[36] Y. Sui, et al., Investigation of optimum mg doping content and annealing parameters of $Cu_2Mg_xZn_{1-x}SnS_4$ thin films for solar cells, Nanomaterials 9 (7) (2019) 1–13, https://doi.org/10.3390/nano9070955.

[37] A. Tumbul, F. Aslan, A. Goktas, M.Z. Zarbali, A. Kilic, Highly stable ethanol-based Cu_2ZnSnS_4 (CZTS) low-cost thin film absorber: effect of solution aging, Mater. Chem. Phys. 258 (2021), 123997, https://doi.org/10.1016/j.matchemphys.2020.123997.

[38] F. Aslan, A. Tumbul, Non-vacuum processed Cu_2ZnSnS_4 thin films: influence of copper precursor on structural, optical and morphological properties, J. Alloys Compd. 612 (2014) 1–4, https://doi.org/10.1016/j.jallcom.2014.05.140.

[39] H. Xie, et al., Formation and impact of secondary phases in Cu-poor Zn-rich $Cu_2ZnSn(S_{1-y}Se_y)_4$ ($0\leq y\leq 1$) based solar cells, Sol. Energy Mater. Sol. Cells 140 (2015) 289–298, https://doi.org/10.1016/j.solmat.2015.04.023. Sep.

[40] A.L. Patterson, The scherrer formula for X-ray particle size determination, Phys. Rev. 56 (10) (1939) 978–982, https://doi.org/10.1103/PhysRev.56.978. Nov.

[41] G.K. Williamson, W.H. Hall, X-ray line broadening from filed aluminium and wolfram, Acta Metall. 1 (1) (1953) 22–31, https://doi.org/10.1016/0001-6160(53)90006-6.

[42] G.K. Williamson, R.E. Smallman, Dislocation densities in some annealed and cold-worked metals from measurements on the X-ray debye-scherrer spectrum, Philos. Mag. 1 (1) (1956) 34–46, https://doi.org/10.1080/14786435608238074.

[43] H. Kafashan, Structural characterizations of pure SnS and In-doped SnS thin films using isotropic and anisotropic models, Mater. Res. Express 5 (4) (2018) 46417, https://doi.org/10.1088/2053-1591/aabdb8.

[44] H. Ahmoum, et al., Impact of preheating environment on microstructural and optoelectronic properties of Cu_2ZnSnS_4 (CZTS) thin films deposited by spin-coating, Superlatt. Microstruct. 140 (2020), 106452, https://doi.org/10.1016/j.spmi.2020.106452.

[45] F. Mikailzade, et al., Structural, optical and magnetic characterization of nanorod-shaped polycrystalline $Zn_{1-x}Mn_xO$ films synthesized using sol–gel technique, Appl. Phys. A Mater. Sci. Process. 126 (10) (2020) 768, https://doi.org/10.1007/s00339-020-03953-0.

[46] Y.B.K. Kumar, D. Nagamalleswari, G.S. Babu, Deposition of Cu_2ZnSnS_4 thin film at different solution flow rates, Phys. B Condens. Matter 645 (2022), 414263, https://doi.org/10.1016/j.physb.2022.414263.

[47] D.M. Berg, "Kesterite equilibrium reaction and the discrimination of secondary phases from Cu_2ZnSnS_4," PhD Dissertation, University of Luxembourg, Faculty of Science, Technology and Communication (FSTC), Physics and Materials Science Research Unit, Luxembourg, 2012.

[48] X. Fontań, et al., In-depth resolved Raman scattering analysis for the identification of secondary phases: characterization of Cu_2ZnSnS_4 layers for solar cell applications, Appl. Phys. Lett. 98 (18) (2011), 181905, https://doi.org/10.1063/1.3587614. May.

[49] J. Tao, et al., Synthesis and characterization of Cu_2ZnSnS_4 thin films by the sulfurization of co-electrodeposited Cu-Zn-Sn-S precursor layers for solar cell applications, RSC Adv. 4 (46) (2014) 23977–23984, https://doi.org/10.1039/c4ra02327g. Jun.

[50] Y. Lin, S. Ikeda, W. Septina, Y. Kawasaki, T. Harada, M. Matsumura, Mechanistic aspects of preheating effects of electrodeposited metallic precursors on structural and photovoltaic properties of Cu_2ZnSnS_4 thin films, Sol. Energy Mater. Sol. Cells 120 (PART A) (2014) 218–225, https://doi.org/10.1016/j.solmat.2013.09.006. Jan.

[51] A. Tumbul, A. Göktaş, M.Z. Zarbali, F. Aslan, Structural, morphological and optical properties of the vacuum-free processed CZTS thin film absorbers, Mater. Res. Express 5 (6) (2018) 66408, https://doi.org/10.1088/2053-1591/aac80e.

[52] P.A. Fernandes, P.M.P. Salomé, A.F.D. Cunha, A study of ternary Cu_2SnS_3 and Cu_3SnS_4 thin films prepared by sulfurizing stacked metal precursors, J. Phys. D. Appl. Phys. 43 (21) (2010), 215403, https://doi.org/10.1088/0022-3727/43/21/215403. May.

[53] P.A. Fernandes, P.M.P. Salomé, A.F. Da Cunha, Study of polycrystalline Cu_2ZnSnS_4 films by Raman scattering, J. Alloys Compd. 509 (28) (2011) 7600–7606, https://doi.org/10.1016/J.JALLCOM.2011.04.097. Jul.

[54] D.M. Berg, et al., Raman analysis of monoclinic Cu_2SnS_3 thin films, Appl. Phys. Lett. 100 (19) (2012), 192103, https://doi.org/10.1063/1.4712623. May.

[55] J. Tauc, Optical properties and electronic structure of amorphous Ge and Si, Mater. Res. Bull. 3 (1) (1968) 37–46, https://doi.org/10.1016/0025-5408(68)90023-8. Oct.

[56] L. Nie, S. Liu, Y. Chai, R. Yuan, Spray pyrolysis deposition and photoresponse of Cu_2CdSnS_4 thin films, J. Anal. Appl. Pyrolysis 112 (2015) 363–368, https://doi.org/10.1016/j.jaap.2014.12.020.

[57] L. Sun, J. He, H. Kong, F. Yue, P. Yang, J. Chu, Structure, composition and optical properties of Cu_2ZnSnS_4 thin films deposited by pulsed laser deposition method, Sol. Energy Mater. Sol. Cells 95 (10) (2011) 2907–2913, https://doi.org/10.1016/j.solmat.2011.06.026. Oct.

[58] A.V. Moholkar, et al., Studies of compositional dependent CZTS thin film solar cells by pulsed laser deposition technique: an attempt to improve the efficiency, J. Alloys Compd. 544 (2012) 145–151, https://doi.org/10.1016/j.jallcom.2012.07.108.

[59] K. Moriya, K. Tanaka, H. Uchiki, Fabrication of Cu_2ZnSnS_4 thin-film solar cell prepared by pulsed laser deposition, Jpn. J. Appl. Phys. Part 1 Regul. Pap. Short Notes Rev. Pap. 46 (9 A) (2007) 5780–5781, https://doi.org/10.1143/JJAP.46.5780. Sep.

[60] A. Alasvand, H. Kafashan, Comprehensive physical studies on nanostructured Zn-doped CdSe thin films, J. Alloys Compd. 789 (2019) 108–118, https://doi.org/10.1016/j.jallcom.2019.03.096.

[61] A. Goudarzi, G.M. Aval, R. Sahraei, H. Ahmadpoor, Ammonia-free chemical bath deposition of nanocrystalline ZnS thin film buffer layer for solar cells, Thin Solid Films 516 (15) (2008) 4953–4957, https://doi.org/10.1016/j.tsf.2007.09.051.

[62] M. Öztaş, M. Bedir, A. Necmeddin Yazici, E. Vural Kafadar, H. Toktamiş, Characterization of copper-doped sprayed ZnS thin films, Phys. B Condens. Matter 381 (1–2) (2006) 40–46, https://doi.org/10.1016/j.physb.2005.12.248.

[63] M.C. Benachour, R. Bensaha, R. Moreno, Annealing duration influence on dip-coated CZTS thin films properties obtained by sol-gel method, Optik (Stuttg) 187 (2019) 1–8, https://doi.org/10.1016/j.ijleo.2019.05.015.

[64] D. Seo, S. Lim, Effect of sulfur and copper amounts in sol-gel precursor solution on the growth, crystal properties, and optical properties of Cu_2ZnSnS_4 films, J. Mater. Sci. Mater. Electron. 24 (10) (2013) 3756–3763, https://doi.org/10.1007/s10854-013-1314-z.

[65] H. Kafashan, R. Ebrahimi-Kahrizsangi, F. Jamali-Sheini, R. Yousefi, Effect of Al doping on the structural and optical properties of electrodeposited SnS thin films, Phys. Status Solidi Appl. Mater. Sci. 213 (5) (2016) 1302–1308, https://doi.org/10.1002/pssa.201532920. May.

[66] A. Jafari-Rad, H. Kafashan, Preparation and characterization of electrochemically deposited nanostructured Ti-doped ZnS thin films, Ceram. Int. 45 (17) (2019) 21413–21422, https://doi.org/10.1016/j.ceramint.2019.07.130.

[67] S. Thanikaikarasan, K. Sundaram, T. Mahalingam, S. Velumani, J.K. Rhee, Electrodeposition and characterization of Fe doped CdSe thin films from aqueous

solution, Mater. Sci. Eng. B Solid-State Mater. Adv. Technol. 174 (1–3) (2010) 242–248, https://doi.org/10.1016/j.mseb.2010.03.054.

[68] R.C. Rai, Analysis of the Urbach tails in absorption spectra of undoped ZnO thin films, J. Appl. Phys. 113 (15) (2013), 153508, https://doi.org/10.1063/1.4801900. Apr.

[69] Y. Natsume, H. Sakata, T. Hirayama, Low-temperature electrical conductivity and optical absorption edge of ZnO films prepared by chemical vapour deposition, Phys. Status Solidi 148 (2) (1995) 485–495, https://doi.org/10.1002/pssa.2211480217. Apr.

[70] A.K. Sen Gupta, E.M.K.I. Ahamed, M. Quamruzzaman, M.A. Matin, K.S. Rahaman, N. Amin, Consequence on Optical Properties of ZnS thin-film deposited by RF magnetron sputtering with varying substrate temperatures, Conf. Rec. IEEE Photovolt. Spec. Conf. 2020-June (2020) 2646–2648, https://doi.org/10.1109/PVSC45281.2020.9300428. Jun.

[71] J. Fu, et al., Improving the performance of solution-processed $Cu_2ZnSn(S,Se)_4$ photovoltaic materials by Cd^{2+} substitution, Chem. Mater. 28 (16) (2016) 5821–5828, https://doi.org/10.1021/acs.chemmater.6b02111. Aug.

[72] M. Tsega, D.H. Kuo, The performance of the donor and acceptor doping in the Cu-rich $Cu_2ZnSnSe_4$ bulks with different Zn/Sn ratios, Solid State Commun. 164 (2013) 42–46, https://doi.org/10.1016/j.ssc.2013.04.006. Jun.